JGR Solid Earth

RESEARCH ARTICLE
10.1029/2018JB016958

The Effect of Wind and Atmospheric Stability on the Morphology of Volcanic Plumes From Vulcanian Eruptions

A. P. Poulidis[1], **T. Takemi**[1], **and M. Iguchi**[1]

[1]Disaster Prevention Research Institute, Kyoto University, Kyoto, Japan

Key Points:
- A database of 896 eruptions from Sakurajima with associated atmospheric profiles is presented
- Different plume bending regimes are quantitatively evaluated using the FPLUME model
- Vertical wind shear mechanically affects plume morphology by aiding or inhibiting plume bending

Supporting Information:
- Supporting Information S1
- Data Set S1
- Data Set S2
- Data Set S3
- Data Set S4
- Data Set S5
- Data Set S6
- Data Set S7
- Data Set S8
- Data Set S9
- Data Set S10
- Data Set S11

Correspondence to:
A. P. Poulidis,
poulidis.alexandros.6z@kyoto-u.ac.jp

Citation:
Poulidis, A. P., Takemi, T., & Iguchi, M. (2019). The effect of wind and atmospheric stability on the morphology of volcanic plumes from vulcanian eruptions. *Journal of Geophysical Research: Solid Earth*, *124*, 8013–8029. https://doi.org/10.1029/2018JB016958

Received 31 OCT 2018
Accepted 28 JUL 2019
Accepted article online 1 AUG 2019
Published online 14 AUG 2019

Abstract Volcanic plumes from small and moderate eruptions represent a challenge in the study of plume morphology due to eruption source parameter uncertainties and atmospheric influence. Sakurajima volcano, Japan, features such activity and due to its continuous eruptions in the recent years provides an ideal natural laboratory. A data set of 896 eruptions between 2009 and 2016 with well-constrained plume heights, estimated erupted mass, and associated atmospheric conditions has been compiled. Plume heights ranged between 1,500 and 5,000 m and mainly developed under stable atmospheric stratification and low background wind speeds. The eruptions presented in the database were used to drive FPLUME, a 1-D integral volcanic plume model, to study the simulated plume morphology. FPLUME was seen to provide consistent results under stable atmospheric stratification. A method for the real-time monitoring of erupted mass used in the Sakurajima observatory was seen to provide appropriate first guess estimates for the eruptions, showing agreement with analytical and simulated mass flow rate calculations. Volcanic plumes from Sakurajima show significant influence by the atmospheric environment. The plume scaling parameter (Π) was used to characterize the expected degree of plume bending with results correlating well against modeled plume angles. The vertical wind profile was seen to have a significant impact on the resolved plume. Wind shear characteristics were seen to have a mechanical effect on the plume, aiding or inhibiting bending. Finally, potential issues were identified in simulations under unstable atmospheric conditions as the model either failed to provide a solution or overestimated the plume height.

1. Introduction

The evolution of a volcanic eruption and the associated secondary hazards is decided by the complex interplay between volcanic and atmospheric factors. The volcanic plume height (H_P) and the associated mass flow rate (MFR or $\dot{M}$) are two key eruptive source parameters (ESPs) for the forecast or hindcast of a volcanic eruption using a Tephra Transport and Dispersal Model (TTDM; Folch, 2012). The relation between the two parameters has been in the center of modern volcanology with analytical models discussed in a number of seminal studies (Sparks, 1986; Wilson et al., 1978; Woods, 1988, among others), which often adapted models based on more general fluid dynamics principles such as the Buoyant Plume Theory (BPT; Morton et al., 1956; Turner, 1969). For strong eruptions (i.e., eruptions featuring a nonbent plume), interactions with the background wind field were initially neglected to construct simplified analytical equations. Even in this simplified setting, volcanic plume behavior is sensitive to a number of source and environmental factors such as vent radius, exit velocity, and density (Woods, 1988) or moisture (Woods, 1993), among others.

In the case of weak eruptions (i.e., eruptions with bent plumes) interactions with the wind field cannot be disregarded, as they can be vital for the reconstruction of plume morphology and the evolution of the eruption (Bonadonna et al., 2015; Bursik, 2001; Degruyter & Bonadonna, 2013; Suzuki & Koyaguchi, 2015; Woodhouse et al., 2013, 2016). In order to accommodate the effect of wind on volcanic plume rise two paths are used: increasingly complex analytical equations, for example, as in Degruyter and Bonadonna (2012), who presented a combined expression based on Morton et al. (1956) and Briggs (1972), or numerical models. Numerical models are further divided to full three-dimensional (3-D) multiphase computational fluid dynamics (CFD) models (e.g., Esposti Ongaro et al., 2007; Herzog & Graf, 2010; Suzuki et al., 2005; Suzuki & Koyaguchi, 2013, 2009) and simplified one-dimensional (1-D) integral models (e.g., Bursik, 2001; de'Michieli Vitturi et al., 2015; Degruyter & Bonadonna, 2012; Devenish, 2013; Folch et al., 2016; Girault et al., 2014;

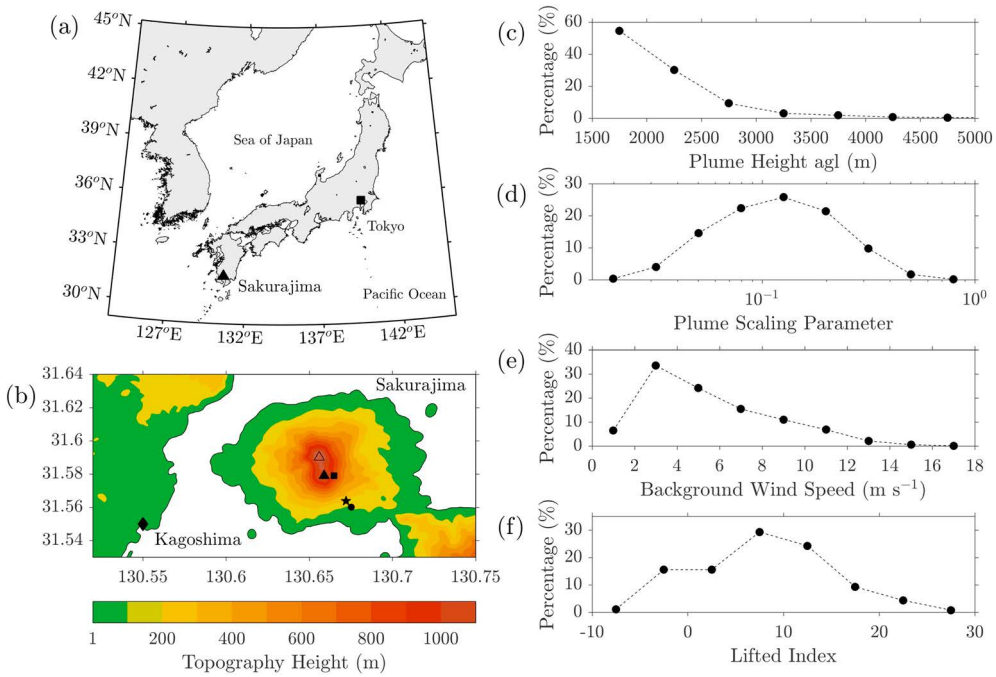

Figure 1. (a) Location of Sakurajima in Japan. (b) Topographic map showing Sakurajima, Kagoshima, the Kitadake (open triangle marker), Minamidake (filled triangle marker), and Showa (circle marker) craters, the seismograph and tilt meter station (star marker), the infrasonic microphone location (circle marker), and the atmospheric sounding station (diamond marker). Topographic contours are shown every 100 m. Right column: Distributions of plume and atmospheric characteristics for the eruptions used in the study: (c) plume height above ground level (agl), (d) plume scaling parameter (Degruyter & Bonadonna, 2012), (e) background wind speed, and (f) lifted index.

Mastin, 2007; Woodhouse et al., 2013). An extensive intercomparison study between 3-D and 1-D models by Costa et al. (2016) showed that, despite their different formulations, both approaches provide reasonably consistent predictions for the key plume characteristics, with results suggesting that 1-D models were relatively better at resolving the morphology of weak plumes.

Here we use FPLUME, a 1-D integral model based on BPT (Folch et al., 2016), in order to study the plume characteristics of small to moderate vulcanian eruptions from Sakurajima volcano, Japan, between 2009 and 2016. Similar studies in the past either concentrated on a few eruptions with well-constrained ESP and meteorological state (e.g., Bonadonna et al., 2015; Costa et al., 2016; Macedonio et al., 2016) or took a stochastic approach in order to study the parameter space (Degruyter & Bonadonna, 2012; Woodhouse et al., 2016). A mixed approach is taken here: ~900 eruptions from Sakurajima are used to study volcanic plume heights and their associated MFR under varying but realistic atmospheric conditions estimated from atmospheric soundings near the volcano (see section 2.1 for more details).

The paper is organized as follows. In section 2 we will briefly introduce Sakurajima volcano, the eruption criteria, and the setup used for the FPLUME model. In section 3 we will present an analysis of the volcanic plume database, followed by the results from the plume modeling with focus on the resolved plume morphology and the influence of the atmospheric state, model sensitivity and briefly discuss cases of non-convergence. Finally, we will discuss the implications of the study, focusing on the differentiation of plume regimes (section 4), before summarizing the main findings in a concluding section (section 5).

2. Location and Methodology

2.1. Sakurajima Volcano

Sakurajima is an andesitic stratovolcano located on the southern rim of the Aira caldera (Aramaki, 1984) on the island of Kyushu in southern Japan (31.58°N, 130.65°E, peak height 1,117 m; Figure 1a). The volcano has two edifices: a dormant edifice on the northern side (Kitadake) and Minamidake, which is the current edifice in the south (Figure 1b). Eruptions from the volcano are typically ash-rich and occur after gas that has been accumulated under a plug of degassed, crystalline magma causes the plug to fail (Iguchi et al.,

2008). Emissions from the volcano affect the air quality (Poulidis, Takemi, et al., 2018) and pose a risk to the surrounding communities (e.g., Hansell & Oppenheimer, 2004; Horwell & Baxter, 2006; Hillman et al., 2012; Jenkins et al., 2015; Lähde et al., 2013; Wilson et al., 2012).

Despite its potential for larger eruptions (Biass et al., 2017; Todde et al., 2017), the volcano has been erupting since 1955 with a series of strombolian (Vergniolle & Mangan M., 2000) and vulcanian (Morrissey & Mastin, 2000) eruptions (Ishihara, 1985; Kinoshita, 1996). The latest eruptive phase started in 2006 with the newly formed Showa crater in the south side of the volcano (Iguchi et al., 2013). Volcanic activity increased toward the end of 2008, and between 2009 and 2015 the volcano was erupting at an almost constant rate: ~80 eruptions per month with plume heights up to 5 km above ground level (agl) leading to ~500 kt of ash ejected per month (see Iguchi et al., 2013 and Poulidis, Takemi, et al., 2018 for a comprehensive analysis). In this study we used eruptions from February 2009 to July 2016.

2.2. ESP and Atmospheric State Estimation

The responsible agency for volcanic hazard management and forecasting is the Japan Meteorological Agency (JMA). The JMA archives eruption details; mainly plume height and some qualitative characteristics (e.g., dispersal axis, eruption size) for observed eruptions. The eruption plume height is estimated using a combination of weather radar data from Fukuoka and Tanegashima (to the north and south, respectively), satellite data (if available), and visual data from a camera near the volcano (Hasegawa et al., 2015; Shimbori et al., 2013).

The volcano is also monitored by the Sakurajima observatory, Disaster Prevention Research Institute at Kyoto University, detailed in Iguchi (2016). In order to monitor magma movement, short-period (1 Hz) three-component seismometers and broadband (frequency range: 0.0083–50 Hz) STS-2 Streckeisen seismometers have been installed in an underground tunnel at Arimura, 2.1 km southeast of the Showa crater (Figure 1b). Horizontal component seismometers are oriented in the direction of the Minamidake crater. A set of two-component radial tangential water tube tilt meters and three-component radial, tangential, and oblique extensometers are installed along 28 m of the underground tunnel. A 7144 ACO infrasonic microphone is installed 300 m south, southeast of the Arimura station in order to detect eruptions at the Showa and Minamidake craters.

Iguchi (2016) proposed a novel method for estimating ejected mass for eruptions from Sakurajima using an empirical relationship between seismological and deformation data:

$$M_T = c_1 A + c_2 V + c_3 \tag{1}$$

where M_T is the ejected material weight (in tons), A is the seismograph spectrum sum between 2 and 3 Hz (m/s), V is the pressure source volume change sum (m^3), and c_3 is a corrective term for reducing noise in seismograph data. The specific values for the parameters ($c_1 = 3.8\times10^{-5}, c_2 = 2.6, c_3 = -1.3\times10^{5}$) were chosen using monthly ashfall data gathered by the Kagoshima prefectural government at 62 locations between 2009 and 2013 so that the Pearson product-moment correlation coefficient is maximized. The method was seen to provide accurate estimates for the total erupted mass for individual eruptions (~10% error) that have been successfully used in specific eruption case studies (Poulidis et al., 2017, 2019). In the rest of the paper this method will be referred to as I2016.

Finally, a JMA weather station is situated in Kagoshima (31.55°N/130.55°E; World Meteorological Organization (WMO) code: 47827). Rawinsondes are launched twice daily (0900 and 2100 Japan Standard Time; JST = UTC + 9). Owing to its proximity to the volcano (~11.25 km to the southwest) sounding data can be used to provide accurate data on the vertical structure of the atmosphere (e.g., temperature, wind, and humidity). Profiles to be used in FPLUME were constructed using sounding data from a subset of the mandatory pressure levels (1,000, 925, 850, 700, 500, 400, 300, and 250 hPa, or ~140–12,200 m agl) to ensure consistency in the data (Poulidis & Takemi, 2017). During the analysis, vertically averaged values for wind speed (U), relative humidity (RH), and temperature (T) were calculated using the four lowest levels (1,000–700 hPa, or ~140–3,100 m agl), while wind speed and wind direction shear values (WSS and WDS respectively) were calculated as the difference between the lower level (140, 800 m agl) and upper level (1,500, 3,100 m) averages. For the sounding indices (e.g., Convective Available Potential Energy, CAPE, and Lifted index, LI), values were used as presented in the archive. Although a number of the indices were studied initially and each index has its own merits (see Blanchard, 1998, for a relevant discussion), only LI was used. LI is calculated as the temperature difference between the environment and an air parcel lifted

adiabatically at 500 hPa and is a measure of atmospheric stability, with negative values indicating instability. As such it provides a measure of atmospheric stability under all conditions (for more details, see section 2.3).

2.3. Eruption Selection Criteria

Observatory records reveal an estimated total number of 14,079 eruptions during the study period. In order to select a consistent and manageable subset, a number of criteria were imposed. First of all, eruptions that did not have a plume height (H_P) assigned by JMA (generally nonexplosive eruptions; Iguchi, 2016) were excluded as H_P is a control parameter. Eruptions that either did not have corresponding atmospheric sounding data or were assigned an RH over 90% were also excluded; the latter to ensure that there is no influence due to cloud cover. Finally, as eruption durations ranged between 1 and 55 min, a smaller subset of eruptions featuring *significant* ($H_P \geq$ 1,500 m agl), *short* ($t_d <$ 10 min) eruptions were chosen; the height limit to allow for the use of sounding data at specified heights, and the duration limit consistency in the plume morphology. A two-tailed Student's t test at a 95–99.9 confidence level revealed that shifting the duration criteria by 5 min (i.e., $6 < t_d < 15$ min) did not produce statistically significant differences in plume heights and atmospheric background parameters. After applying the above criteria a total number of 896 eruptions were used to run the FPLUME model. The list of plume heights, estimated MFR, and the atmospheric profiles can be found as supporting information (Data Sets S1–S3).

2.4. Quantifying Wind Impact

Traditionally, two plume regimes were identified based on eruption intensity and wind strength: strong (Bonadonna & Phillips, 2003) and weak (Bursik, 2001). Recently, an additional regime has been identified between these two extremes, with *distorted* (Carazzo et al., 2014) or *transitional* (Bonadonna et al., 2015) plumes. Here we adopt this three-regime approach. Specifically, we will use the plume angle to broadly categorize the plumes, with values ≤30° from the horizontal denoting weak plumes, ≥60° strong plumes, and values inbetween transitional plumes.

Two scaling parameters have been introduced to quantify the impact of wind on plume rise: the "plume scaling parameter" (Π; Degruyter & Bonadonna, 2012) and the "dimensionless time scale" (τ^*; Carazzo et al., 2014). The first is expressed as the ratio of plume height expressions proposed for a purely buoyant plume released into a calm atmosphere (strong plume; Morton et al., 1956) and a plume rising in a cross-flow (weak plume Briggs, 1972) in order to assess the amount plume bending, calculated as

$$\Pi = \frac{\bar{N} H_P}{1.8 \bar{N}} \left(\frac{\alpha}{\beta} \right)^2 \underset{\beta=0.5}{\overset{\alpha=0.1}{\approx}} 0.022 \frac{\bar{N} H_P}{\bar{U}} \tag{2}$$

where N is the buoyancy frequency, with bars denoting averages between the surface and plume top (here between 1,000 and 700 hPa), while α and β are the streamwise and cross-flow air entrainment coefficients, respectively (see section 2.5 for details). For the calculation of Π we assumed $\alpha = 0.1$ and $\beta = 0.5$ which are typical values and were close to the averages along the plume axis output by FPLUME ($\alpha = 0.14 \pm 0.03$, $\beta = 0.53 \pm 0.06$).

Increasing values of Π indicates increasingly stronger plumes. Bonadonna et al. (2015) suggested Π threshold values of 0.1 (weak to transitional) and 10 (transitional to strong). In analog experiments carried out by Carazzo et al. (2014) it was seen that the thresholds were, respectively, ~0.06 and ~0.2, suggesting that a value of 10 might be overstated. This can also be seen in the case of plumes from Sakurajima volcano: for a stable atmosphere ($\bar{N} = 0.01$ s^{-1}) and very low wind speed ($\bar{U} = 1$ m/s), a Π value of 1 is the maximum that can be achieved for plume heights studied here ($H_P \leq$ 5,000 m).

Carazzo et al. (2014) followed a different approach by addressing the fundamental time scales associated with vertical and horizontal motions at play and introduced τ^* as

$$\tau^* = \frac{\tau_v}{\tau_h} \equiv \frac{H_0(\alpha, \dot{M}, \bar{N})/U_0}{H_1/\bar{U}} \tag{3}$$

where τ_v and τ_h are the vertical and horizontal time scales, respectively, H_0 is the natural length scale of a plume rising in a calm, stratified environment (Morton et al., 1956), H_1 is a reference altitude over which wind acts (e.g., the tropopause) and U_0 is the jet velocity. Tested in a series of analog experiments, τ^* was seen to provide an accurate estimate for the maximum plume height irrespective of plume bending. In the case of τ^* small (large) values indicate strong (weak) plumes,that is, the opposite compared to Π.

Both parameters have a similar basis, representing a ratio between the strength of horizontal and vertical effects on the plume; however, the key diagnostics used are different: more suited for an observational setting for Π (N, H_P, U) and more suited as control parameters in an experimental setting for τ^* ($\dot{M}$, U_0). Both parameters, directly or indirectly, require the definition of either α (τ^*) or both α and β (Π), but in the case of Π uncertainty in the coefficients produces a larger potential for error due to the square dependence. For the main bulk of the analysis here Π will be used to assess bending in the plume as the required diagnostics can be estimated from the atmospheric sounding data; however, the ability of both parameters in assessing the plume height and plume bending regime will be addressed in section 4.

2.5. FPLUME Model Setup

FPLUME is a 1-D steady state volcanic plume model based on the BPT (Folch et al., 2016) and is commonly coupled with the FALL3D TTDM (Costa et al., 2006; Folch et al., 2009). The model considers the plume as a multiphase mixture of volatiles, suspended tephra, and entrained ambient air. Water (in all phases) is the only volatile species considered, irrespectively of the origin (magmatic, phreatic or from the injection of ambient air). Assumptions in the formulations of BPT only hold for the region below the Neutral Buoyancy Level (NBL), and as such a semiempirical approach is used above that. For a full description of the governing equations and parameterizations, see Folch et al. (2016) and Macedonio et al. (2016).

The correct estimation of the entrainment of ambient air into the plume is critical when modeling volcanic plumes (Bursik, 2001; Folch et al., 2016; Macedonio et al., 2016; Suzuki & Koyaguchi, 2015). Entrainment in the model is controlled by two key coefficients for streamwise and cross-flow entrainment (α and β, respectively). FPLUME features two schemes for the estimation of α (*Kaminski-C* and *Kaminski-R*; Kaminski et al., 2005) and one for β (*Tate*; Tate & Middleton, 2000; Tate, 2002), with an additional choice being the selection of a constant value (typically $\alpha \in [0.05,0.15]$ and $\beta \in [0.1,1]$). The two schemes for α follow the same formulation (introduced by Kaminski et al., 2005), but differ based on the experimental data used to determine the required constants, while the scheme for β uses a simple formula based on laboratory experiments (see Folch et al., 2016, and references therein).

Other than the entrainment coefficients, the model allows for several options for plume bending (Bursik, 2001), fallout of particles from the plume (Bursik, 2001), particle terminal velocity (Ganser, 1993), particle reentrainment (Ernst et al., 1996), water phase changes (Woods, 1988, 1993), particle aggregation (Brown et al., 2012; Costa et al., 2010), and column collapse. All available options were used aside from particle aggregation. Although aggregation is known to be an important process in Sakurajima (Bagheri et al., 2016; Gilbert & Lane, 1994) and the total grain size distribution (TGSD) of each eruption is known to impact plume height (Macedonio et al., 2016; Michaud-Dubuy et al., 2018), owing to the lack of concrete data and the large span of the study period, the TGSD used is the one assigned to Sakurajima by Mastin et al. (2009), that is, 0.24, 0.25, 0.2, 0.12, 0.09, 0.0425, 0.0325, 0.0125, 0.0075, and 0.005 for ϕ ranging between −1 and 8 ($\phi = -\log_2(d)$ in millimeters).

The majority of the simulations are carried out using H_P as the input parameter, solving for MFR. The limits for MFR were set between 10^2 and 10^7 kg/s in order to cover a realistic parameter space. A subset of simulations was carried out using the I2016 MFR as input (see section 3.4 for details). Exit velocity values (u_0 = 70, 120, 170 m/s) were based on previous studies in Sakurajima (Suwa et al., 2014; Tournigand et al., 2017), while exit temperature (T_0 = 1150, 1250, 1350 K) and water fraction (w_0 = 1%, 3%, 5%) were chosen to represent limits commonly used in the literature (e.g., Costa et al., 2016 and Macedonio et al., 2016). For most of the analysis presented here we use a "control" set with u_0 = 120 m/s, T_0 = 1, 250 K, w_0 = 3% and the Kaminski-C and Tate parameterizations. Sensitivity tests were carried out for all combinations of u_0, T_0, w_0, and the two Kaminski parameterization schemes, while three additional sets of simulations were carried out using a constant value for the cross-wise air entrainment coefficient (β = 0.1, 0.5, and 1), leading to a total of 57 sets of 896 eruptions or 51,072 simulations.

3. Results

3.1. Database Analysis

The distributions of the plume and atmospheric background parameters are shown in Figures 1c–1f. The majority of the eruptions (489 or 54.6% of the total sample) feature H_P between 1,500 and 2,000 m (Figure 1c). The percentage decreases drastically for eruptions with taller plumes down to two eruptions (0.2%) for H_P between 4,500 and 5,000 m. Based on Π values, most of the eruptions in Sakurajima are expected to be

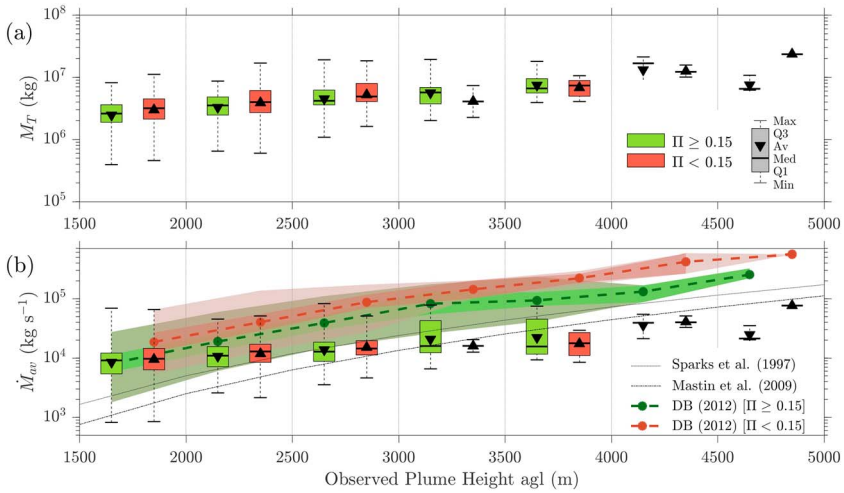

Figure 2. (a) Box-and-whiskers plot of total estimated mass based on Iguchi (2016) against observed plume height above ground level, with different colors based on plume scaling parameter. Box plots are staggered for visibility but correspond to the same plume heights (1,500–2,000 m, etc.). (b) Box-and-whiskers plot of mean mass flow rate against observed plume height above ground level. Dashed lines are estimates based on Degruyter and Bonadonna (2012) (shown as "DB (2012)") with the shaded areas showing the interquartile range (bright green and red) and the minimum to maximum range (pale colors), while the dot and dash-dotted lines are estimates based on Sparks et al. (1997) and Mastin et al. (2009), respectively. Note the logarithmic scale in the *y* axis.

significantly influenced by the wind, with values distributed in a Gaussian fashion around 0.1 when plotted on a logarithmic scale (Figure 1d). During the initial part of the analysis we use a limit of $\Pi = 0.15$ to split the set to two manageable subsets. This was arbitrarily chosen as it led to a better separation of plume characteristics (see Figures 2 and 3). The appropriate limits between the weak, transitional, and strong plume regimes for the eruptions studied are discussed in detail in section 4.

Background wind speed is, on average, relatively low with 40% of the eruptions associated with $U \leq 4$ m/s (Figure 1e). Still, a significant amount of eruptions (~10%) occurred under strong background winds ($U \geq 10$ m/s). The majority of eruptions are associated with stable atmospheric stratification with an average LI of 8.1 (Figure 1f). However, ~32.1% occurred under low stability or unstable conditions. These values are very close to the climatological values for the Kyushu island shown in Poulidis and Takemi (2017), where it was seen that for almost half of the year atmospheric flow is dominated by westerly winds and high stability, while a high probability for atmospheric instability occurs during the late summer and early autumn months.

The total erupted mass for each eruption (estimated using equation (1)) is shown in Figure 2a. For the analysis, plume heights were split into seven bins at a 500-m interval, from 1,500–2,000 m up to 4,500–5,000 m and further separated based on Π. Overall the estimated M_T values range between 10^5 and 10^7 kg (volcanic explosivity index (VEI) 2–4), which is the expected range for strombolian and vulcanian eruptions (Newhall & Self, 1982). At low H_P these results show significant spread, with a single H_P bin corresponding to 2 orders of magnitude of M_T values. Looking at the interquartile range (IQR, i.e., ~50% of the data around the median value, between the first (Q1) and third (Q3) quartiles) restricts M_T values to 1 order of magnitude. As expected higher H_P values correspond to larger M_T values. The spread around the mean and median decreases with increased H_P, but this is mainly due to the decrease in the sample size. As expected eruptions with $\Pi < 0.15$ require larger M_T values to reach the same plume height; however, the differences are relatively small.

The average MFR ($\dot{M}_{av}$) was calculated by dividing M_T with t_d (estimated as the time from the eruption until the seismic signal returned to background levels). This is shown in Figure 2b, along with MFR estimates based on Sparks et al. (1997), Mastin et al. (2009), and Degruyter and Bonadonna (2012) (see the individual references for details). Results for the latter are calculated for the 896 eruptions and separated into two groups at $\Pi = 0.15$. These methods will be referred to as S1997, M2009, and DB2012 for the rest of the paper. As MFR is known to fluctuate significantly between different orders of magnitude in the time scales of seconds to minutes, especially in short eruptions (Clarke et al., 2002; Tournigand et al., 2017), the estimates

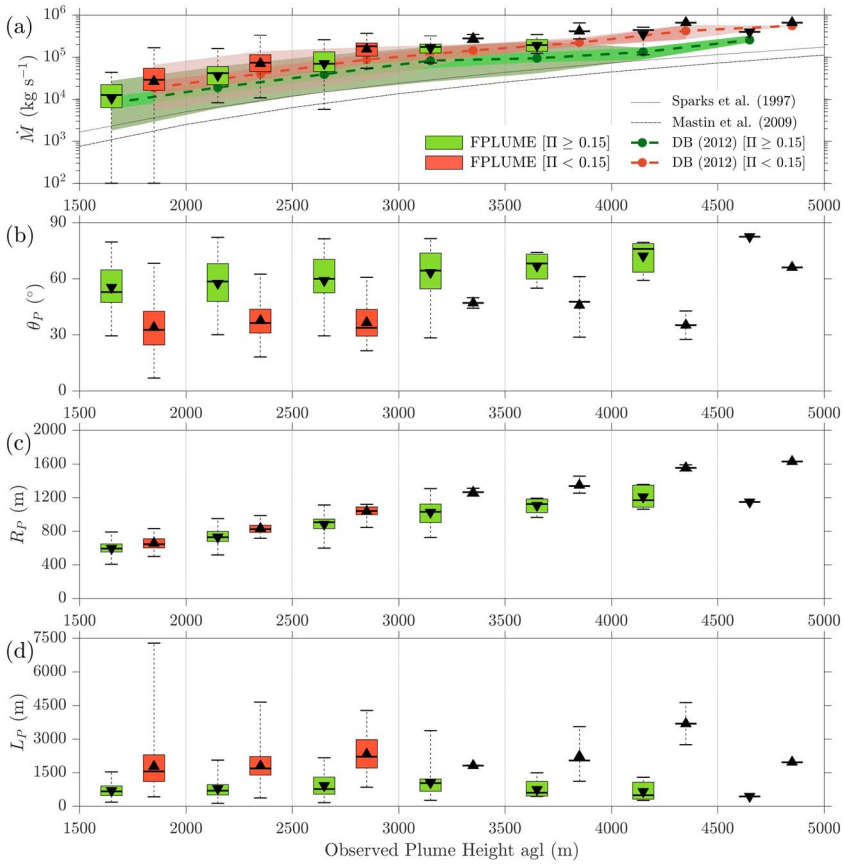

Figure 3. Box-and-whiskers plots of plume characteristics as simulated by FPLUME against observed plume height above ground level: (a) mass flow rate ($\dot{M}$), (b) plume angle (θ_P), (c) plume radius (R_P), and (d) plume length (L_P). Note the logarithmic scale in the y axis of panel (a). The extra lines shown in (a) follow Figure 2.

from the three analytical models are closer to the peak MFR required for a specific H_P and can be expected to differ from $\dot{M}_{\text{av}}$.

A comparison reveals that estimates among the various methods vary depending on H_P. For low H_P (1,500–2,000 m) and for stronger plumes ($\Pi \geq 0.15$) the estimates using DB2012 are close to $\dot{M}_{\text{av}}$ by I2016, but with a more significant gap between the two Π groups. At these H_P values S1997 and M2009 provide an estimate at the lower end of the I2016 estimates. For taller plumes (>4,000 m), results are notably different: DB2012 estimates are between 1 and 2 orders of magnitude higher than the I2016 estimates, suggesting that for larger eruptions the range of instantaneous MFRs that are essentially being averaged has a large impact. The S1997 and M2009 estimates are comparable to the I2016 averages, but are closer to the upper limits.

Overall, considering the difference in the formulation and assumptions behind DB2012 and I2016, results from the two methods are remarkably close. It is worth noting that in all cases the DB2012 estimates fall between the I2016 $\dot{M}_{\text{av}}$ and M_T estimates, which can thus be used to provide lower and upper limits for first guess estimates.

3.2. Simulated Plume Characteristics

A total of 57 sets of the 896 eruptions were used to run the FPLUME model. For the most part results from the "control" configuration will be discussed here, unless noted otherwise. Although results differ slightly per set, in approximately 85% of the eruptions convergence succeeded and the model produced a solution. The failed convergence cases will be examined in section 3.4. The model outputs a number of plume-related parameters along the plume axis, including plume angle (θ_P), radius (R_P), length (L_P), density, temperature, velocity, α, β, and plume composition. Here, aside from the plume height, we focus the analysis on three parameters: minimum θ_P, maximum R_P, and horizontal L_P (the distance between the vent and the end of

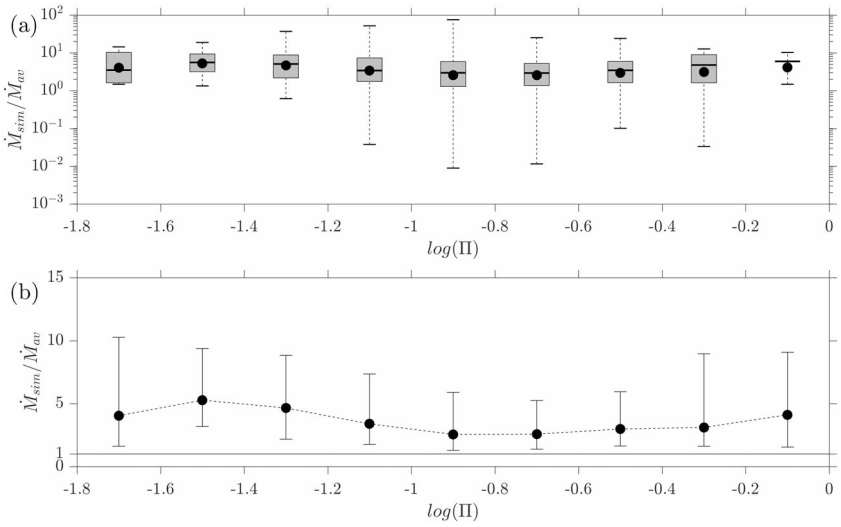

Figure 4. (a) Box-and-whiskers plot of the simulated to estimated average mass flow ratio against the plume scaling parameter (Π). (b) As in (a) but showing only average values and error bars based on the first and third quartiles. Note the logarithmic scale in the *y* axis of panel (a).

the plume). Note that the plume angle shown is *with respect to a horizontal surface*, so a value of 90° denotes a straight plume. Full results are included as supporting information (Data Sets S4–S10).

A comparison between FPLUME results and analytical solutions for MFR (S1997, M2009, and DB2012) is shown in Figure 3. Comparing FPLUME results and DB2012 estimates reveals strikingly similar results, both for the average and median values as well as the IQR and minimum to maximum ranges, and show a similar gap between the two Π groups. Similar to the 1-D model to analytical solution comparison presented by Degruyter and Bonadonna (2012), the agreement partially breaks down at low plume heights (1,500–2,000 m), but only when considering the range between the minimum and the Q1 values. As seen in Figure 2, the S1997 and M2009 estimates are low-end estimates, again mirroring the results in Degruyter and Bonadonna (2012).

Plume angles are broadly as expected for the given Π values. For plume heights up to 4,500 m, there is a very clear separation between the weaker ($\Pi < 0.15$; $\bar{\theta}_P$ ranging between 33.8° and 47°) and stronger plumes ($\Pi \geq 0.15$; $\bar{\theta}_P$ between 55.3° and 72°). The gap between the two groups is more narrow for plumes between 4,500 and 5,000 m, but there is still a 16.4° difference.

Results for R_P do not vary significantly between the two groups for low plume heights (<3,000 m), with an average difference of 100–200 m. However, the gap between the two groups is significantly larger for taller plumes, as the weak plume R_P values taper off after 3,000 m, while the stronger ($\Pi \geq 0.15$) plume R_P values increase with plume height, leading to a final difference of 482 m (Figure 3c).

Finally, results for the L_P also show a systematic difference between the two regimes, with average values ranging between 1.7–3.6 km for the weak and 0.4–1.1 km for the transitional plumes (Figure 3d). Note that in the case of $\Pi < 0.15$ the horizontal length of plumes tends to be comparable to the plume height. Overall, the values of L_P make physical sense, although for the very low H_P some of the estimated model values might be overestimated, leading to plume length to height ratios of more than 3, with a maximum ratio of 4.6.

During an eruption our goal would be to use the I2016 estimate in real-time to drive forecast simulations. To further examine the relation between the estimated (from I2016) and the simulated (FPLUME) MFR values, the ratio between the FPLUME simulated MFR ($\dot{M}_{\mathrm{sim}}$) and I2016 estimation ($\dot{M}_{\mathrm{av}}$) was calculated (Figure 4) and plotted against Π (Figure 4). When all values are taken into account the ratio shows that simulated and estimated MFR values can differ by as much as 4 orders of magnitude (Figure 4a). Specifically for Π values close to 0.1, the simulated value is less than the estimate, suggesting that, as far as the model is concerned, $\dot{M}_{\mathrm{av}}$ is an overestimate. However, only focusing on the IQR shows that for ~50% of the eruptions studied, the ratio is generally constrained within an order of magnitude, with an average value of 3.6 (Figure 4b).

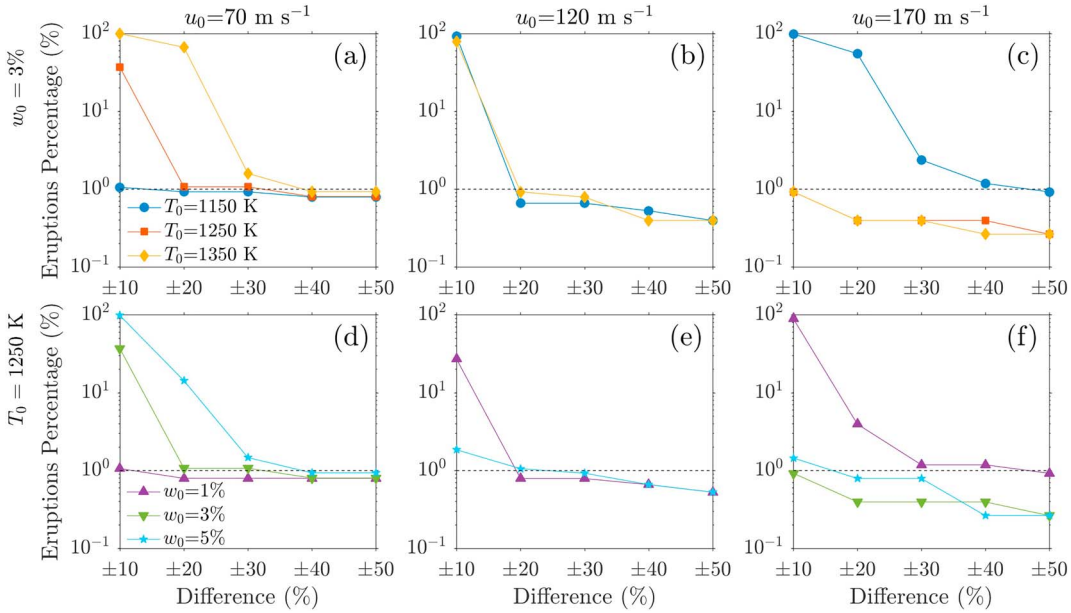

Figure 5. Model sensitivity for the calculation of the mass flow rate to eruption parameters shown as change percentage against the percentage of eruptions affected. First row: set exit water vapor (w_0 = 3%) and exit temperature (T_0) ranging between 1,150 and 1,350 K (different colors) for exit velocity (u_0) values of: (a) 70 m/s, (b) 120 m/s, (c) 170 m/s. Second row: set $T_0 = 1,250$ K and w_0 ranging between 1% and 3% (different colors) for u_0: (d) 70 m/s, (e) 120 m/s, (f) 170 m/s. All combinations are compared against a control configuration (w_0 = 3%, $T_0 = 1,250$ K, u_0 = 120 m/s). The horizontal dashed line denotes 1% of the total eruptions studied. Note the logarithmic scale in the y axis.

Up to this point, only results from the "control" set were considered. For weak eruptions, the FPLUME model is known to be relatively insensitive to changes in the exit parameters for the eruptions (i.e., u_0, T_0, and w_0), with the largest sensitivity seen for α and β (Macedonio et al., 2016). Similar results were seen in the simulations presented here: Figure 5 compares the MFR values calculated from the control set against other parameter combinations, with the difference between the sets shown as a percentage (x axis) against the percentage of eruptions that the change occurred (y axis). For the comparisons either w_0 or T_0 was held at a set value in order to check the sensitivity to u_0 and the unheld parameter. In all cases results show that the different combinations only accounted for a 10–20% change in the simulated MFR, with less than 1% showing a change of more than 50%. Considering that MFR changes are usually considered in different orders of magnitude we can conclude that the model is largely insensitive in the parameter space checked here. Similar results where seen for the two schemes used for α (see Figure S1 and Table S1). On the other hand, specifying constant values for β was seen to significantly affect plume characteristics (Figure S2 and Table S2), mirroring previous results from Macedonio et al. (2016). Overall, the model uncertainty due to the unknown exit parameters was approximately 5% for the morphological characteristics of the plume and 10–30% for the MFR.

3.3. Atmospheric Influence

Although the atmospheric impact on the morphology of the plume is well-established (e.g., Bursik, 2001; Bonadonna et al., 2015), the impact of the detailed cross-flow wind vertical profile has only recently begun being investigated (Girault et al., 2016; Suzuki & Koyaguchi, 2015; Woodhouse et al., 2016)). An important conclusion has been that wind speed shear (WSS; a change of wind speed with height) can enhance the rate of turbulent entrainment in the plume, which can lead to decreased plume heights (Girault et al., 2016; Woodhouse et al., 2016). Here, along with WSS, we study the influence of another wind shear parameter, the vertical wind direction shear (WDS), both parameters that have also been shown to affect ash deposition (Michaud-Dubuy et al., 2019; Poulidis, Phillips, et al., 2018), as well as LI as a measure of instability in the atmosphere. Results are presented for the two end members of the distribution for each parameter (i.e., ~50% that lies within the minimum and Q1 and Q3 to maximum ranges) in order to have a clear measure of the largest impact of each parameter. A two-tailed Student's t test comparing the upper and lower ranges revealed statistically significant changes for WSS, WDS, and LI.

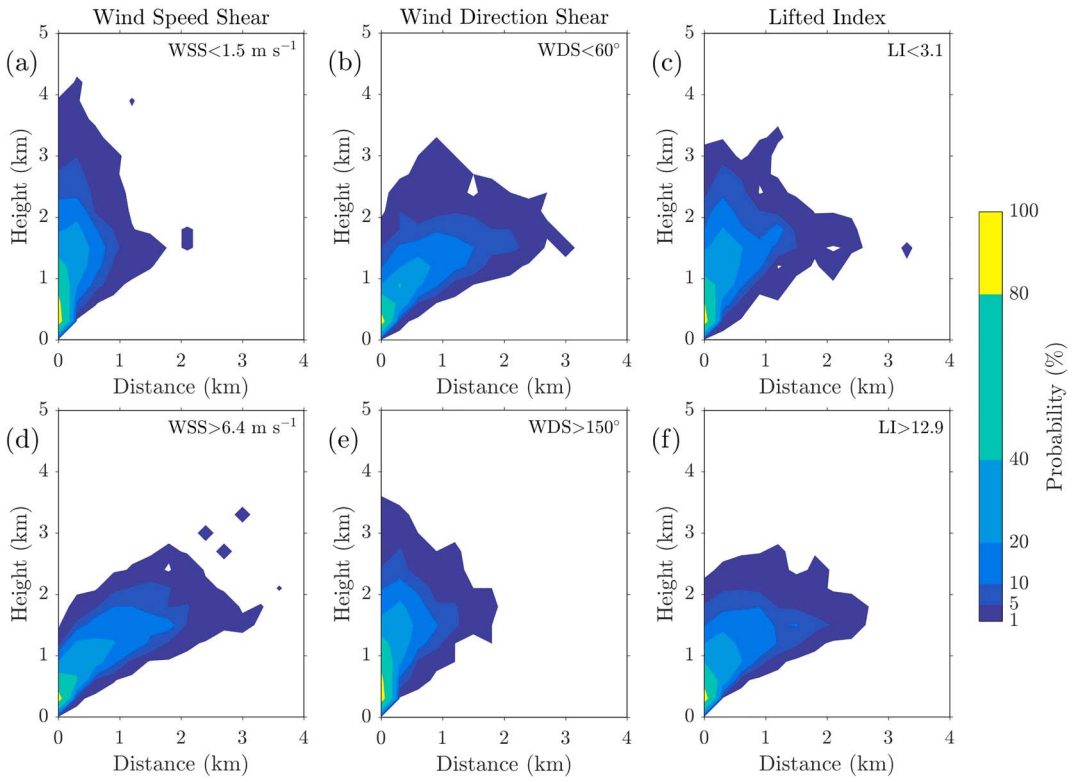

Figure 6. Probability density diagrams showing simulated plume shape for different environmental stability parameters: (a, d) wind speed shear (WSS), (b, e) wind direction shear (WDS), and (c, f) lifted index (LI). For each parameter the distribution is shown for eruptions with parameter values below the first quartile (a–c) and above the third quartile (d–f).

Probability density diagrams (PDD) of the plumes in each category are shown in Figure 6, while average morphological characteristics are shown in Table S3. Note that the PDDs were created only using the plume axis (i.e., ignoring the radius). Low WSS is generally associated with stronger plumes ($\bar{\theta_P} = 57°$), while high WSS acts to tilt the top of the plume ($\bar{\theta_P} = 27°$) and is more readily associated with bent plumes (compare Figures 6a and 6d), leading to a decrease in the average plume height by 221 m. On the other hand, low WDS allows for plume bending ($\bar{\theta_P} = 34°$; Figure 6e), which is partially negated in the cases of high WDS ($\bar{\theta_P} = 50°$; Figure 6e), leading to an increase of the average plume height by 168 m. In this respect, the two wind shear parameters can thought to have a mechanical effect on the plume, tilting (high WSS) or supporting (high WDS) the upper part of the plume. The effect of LI is more subtle, as low LI values generally allow for higher plumes (283 m plume height difference on average) but affects plume bending to a lesser extent of the wind shear parameters, associated with an 9° difference on average (Figures 6c, 6f, and Table S3). Plume length also varies accordingly, with longer plumes associated with higher plume bending, but the plume radius is affected to a lesser degree, with the largest changes at 68 m in the case of LI (Table S3). Moisture is known to have a significant impact on plume height (Degruyter & Bonadonna, 2012; Woods, 1993). However, in the range checked here (RH∈[0,90%]) results were not statistically significant, suggesting that higher ambient RH values (~100%) would be required for plume heights to be significantly affected.

Similar conclusions can be drawn from scatter plots of the morphological plume characteristics against Π (Figure 7). Although the distribution of low and high value cases for all three parameters against Π shows some overlap, conditions that are associated with more plume bending tend to have lower Π values (see the distribution of cases against the x axis in Figures 7a–7c) and lower H_P. As with Figure 6, the clearest distinction between the low- and high-parameter cases is seen for θ_P, where the different subsets can be associated with significantly different logarithmic approximations (Figures 7d–7f). The most distinct case is for WSS, where the θ_P values for the high and low subsets are separated at the 40° angle (Figure 7d). Cases with high WSS are associated with low θ_P values even for stronger plumes (Π ~0.4). In this sense looking at WSS can

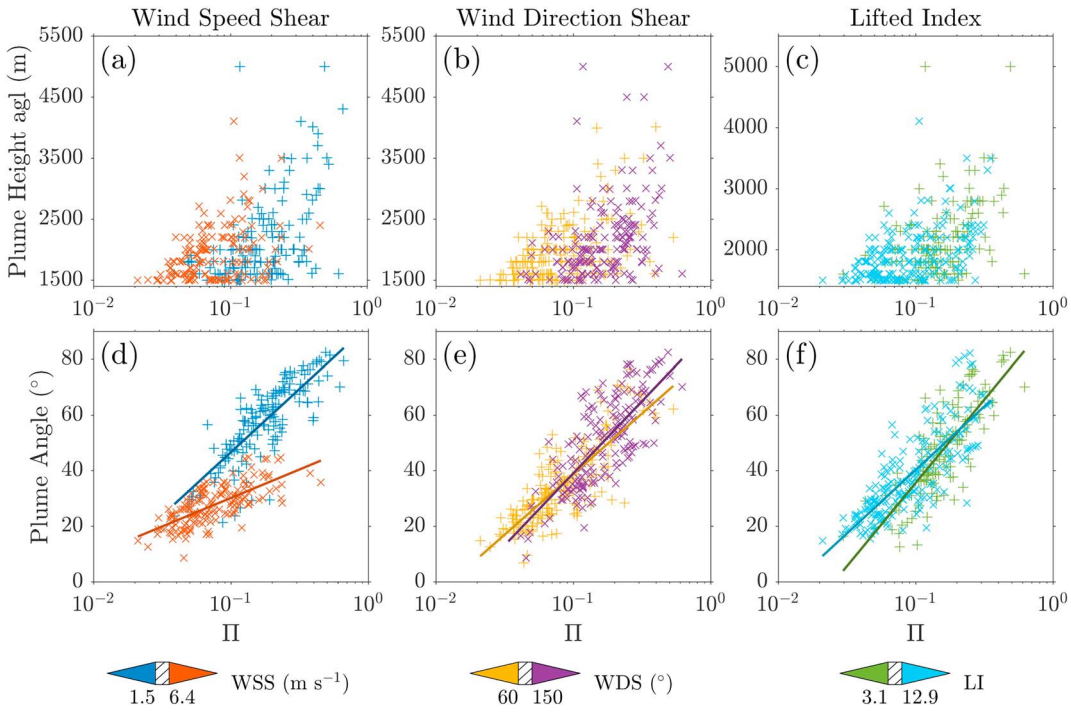

Figure 7. Plume characteristics against Π for different environmental stability parameters: (a)–(c) plume height, and (d)–(f) plume angle. Plume characteristics are shown for wind speed shear (WSS, first column), wind direction shear (WDS, second column), and L I (third column), with the different marker colors showing eruptions with parameter values below the first quartile and above the third quartile. In panels (d)–(f) logarithmic approximations are plotted using darker colors over the respective data.

help provide disambiguation in cases an observed plume does not match the characteristics of its estimated Π value (e.g., a bent plume with a high Π value). Similar conclusions can be drawn for WDS, although the distinctions between the two subsets is less clear (Figure 7e). As noted when discussing Figure 6, LI does not have as clear an impact on the plume angle as the other two parameters (a 9° difference between the two subsets). This can also be seen in Figure 7f; the fact that low LI values are generally associated with Π values over 0.1 means that, on average, θ_P values also tend to be higher, but there is no clear separation between the two subsets.

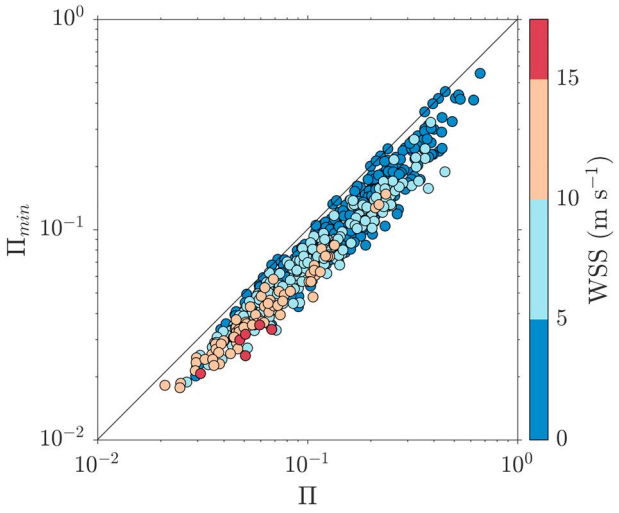

Figure 8. Scatter plot of Π_{min} against Π values. Coloring depends on wind speed shear as shown in the color bar. Note that both axes use a logarithmic scale. WSS = wind speed shear.

In the case of WSS an additional parameter that could be used alongside Π to provide disambiguation would be Π_{min}, following the same formula as Π but using the maximum, not average, values of N and U. Substantial differences between Π_{min} and Π would point toward the existence of a shear layer with significant impact (Figure 8). However, due to the invariability of Π calculations to wind direction, the effect of WDS would have to be accounted for in a case-by-case basis—a fact particularly important in the case of Sakurajima as strong wind direction shear is a common feature, especially during the late summer months (Poulidis & Takemi, 2017).

3.4. Failed Convergence Cases

As pointed out in section 3.2, in approximately 15% of the eruptions, the model failed to find a solution in the given parameter space. Distributions describing the atmospheric state for these eruptions is shown in Figure 9. The distributions of LI and Π for the successful cases (Figures 9a and 9c) are very similar to those for the whole sample (Figures 1f an 1d, respectively), showing that the absence of the failed cases does not have a significant effect on the results described in section 3.3. However, focusing on the cases of failed convergence shows that they are actually

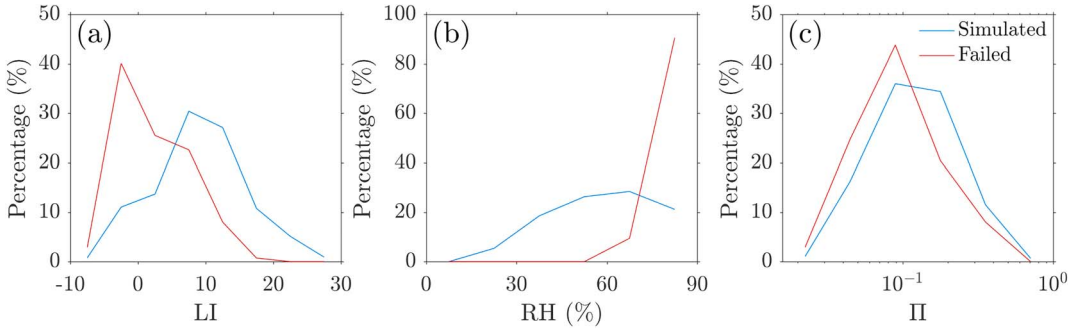

Figure 9. Distribution of atmospheric structure and eruption characteristics for simulations in which convergence succeeded (blue) and failed (red) against: (a) lifted index (LI), (b) relative humidity (RH), and (c) plume scaling parameter (Π).

a specific subgroup within the whole eruption sample that features unstable atmospheric conditions: low atmospheric stability (i.e., low to negative LI values; Figure 9a) and high relative humidity (RH> 80%; Figure 9b), typically with slightly lower Π values (Figure 9c).

In order to see whether this issue persists for the inverse problem, simulations for the failed cases were carried out using FPLUME with the I2016 MFR estimates ($\dot{M}_{av}$) as input and H_P as output (included as supporting information Data S11). Out of the 137 simulations carried out 75 succeeded, while 62 failed. Results for the simulated plume height and length are shown in Figure 10a. Simulations that succeed under these unstable conditions generally provide overestimates for the plume height, with an average model to observations ratio of 1.1 and a maximum of 4.6. Simulations that overestimate H_P also tend to be associated with unnaturally long plumes in the model, with the maximum resolved L_P at 22.7 km, making this a diagnostic that could be used as a straightforward check on whether a solution should be trusted or not. Overall, results show that under a very unstable atmosphere the model tends to overestimate plume rise. On H_P to MFR calculations, this would mean that the model would underestimate the MFR in order to accommodate a short plume, suggesting that this could be one of the reasons for the mismatch between FPLUME results and DB2012 estimates seen in Figures 3 and 4. Note that for the short plumes studied here an additional issue might be the lack of detail in the lower levels of the vertical atmospheric profile.

As an alternative for these unresolved cases, H_P estimates were calculated using the formulas suggested by Morton et al. (1956) ($H_P \propto \dot{M}^{1/4}N^{-3/4}$) and Briggs (1972) ($H_P \propto \dot{M}^{1/3}N^{-2/3}U^{-1/3}$; see Degruyter and Bonadonna (2012) for a relevant discussion). Using the same MFR values and $\alpha = 0.1$, $\beta = 0.5$ for the air entrainment coefficients, both equations were seen to provide consistent estimates for plume height

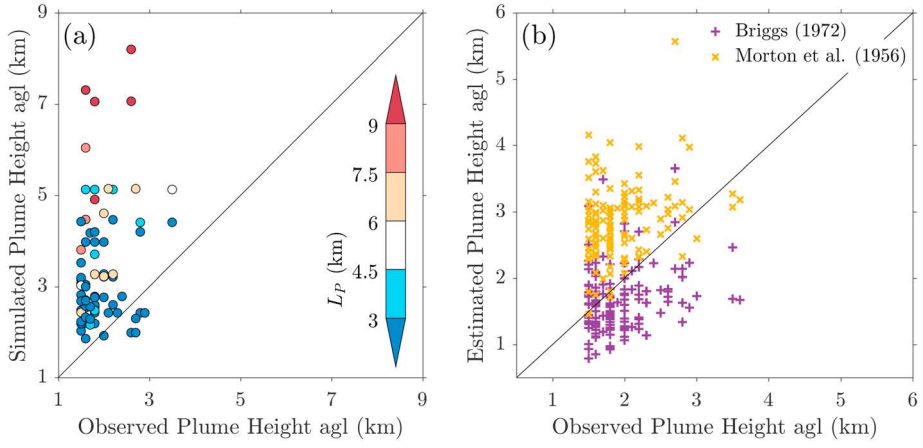

Figure 10. (a) Simulated plume height using FPLUME against observed plume height based on failed simulations, but solving for plume height using I2,016 mass flow rate estimates. Marker color is based on the plume length (L_P). (b) Estimated plume heights using analytical equations suggested by Morton et al. (1956) and Briggs (1972) against observed plume height based on failed simulations.

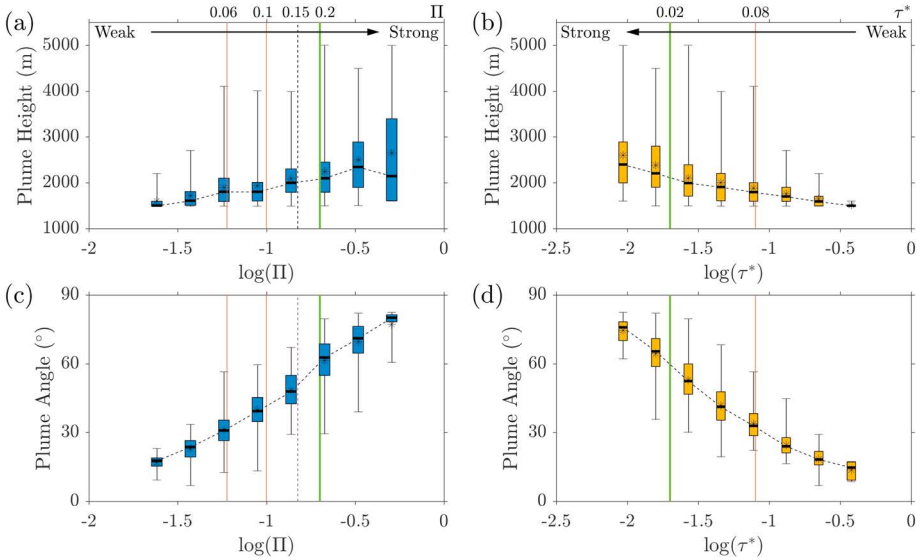

Figure 11. Plume characteristics against the logarithm of scaling parameters: (a, b) plume height, (c, d) plume angle. Different box colors shown to differentiate between Π (blue) and τ^* (yellow). Dashed lines are used to connect median values. In the left column, the vertical lines indicate the regime change between weak and transitional plumes (thin orange lines; based on Carazzo et al., 2014 and Bonadonna et al., 2015), and transitional to strong (thick green line, based on Carazzo et al., 2014), while the dashed line shows the limit used in the current study for reference. In the right column, the limits shown are based on Carazzo et al. (2014).

(Figure 10b). As expected considering the Π regime under study, Briggs (1972) provides better estimates, with a slight underestimation (average ratio of 0.89), while Morton et al. (1956) generally overestimates values (average ratio of 1.54). The best match between estimates and observations was obtained using a weighted average between the two methods (0.85 factor for Briggs, 1972, and 0.15 factor for Morton et al., 1956), which led to an average ratio of 0.99 (not shown in the figure).

4. Plume Regime Separation

In the analysis presented, use of Π was tested in a number of eruptions with different atmospheric settings. An arbitrary threshold value of $\Pi = 0.15$ was to separate the data into two categories with distinct characteristics; however, the limits between the three plume regimes discussed in Carazzo et al. (2014) and Bonadonna et al. (2015), that is, weak, transitional, strong, were not examined in detail. This will be discussed here for the Π and τ^* parameters.

As mentioned in section 2.4, the calculation of τ^* requires knowledge of diagnostics not directly observable in the eruptions studied here, mainly U_0—the velocity of the jet. Here in order to account for this output from control set of the FPLUME simulations is used. Specifically U_0 is set as the plume velocity over the vent. This depends on the exit velocity (that is set to 120 m/s) but also takes into account the effect of the atmospheric and eruptive state, which leads to some variability in the results. Furthermore, for the reference height (H_0), instead of the tropopause height (as suggested by Carazzo et al., 2014) we used $3H_{\mathrm{NBL}}$, where H_{NBL} is the height of the NBL (again determined by FPLUME). This was done to better capture the layer over which the wind had a strong influence over the relatively short plumes studied here and was seen to provide values that matched well against results from Carazzo et al. (2014). Results for the two parameters were split into eight groups and are presented against H_P and θ_P (Figure 11).

The two parameters, although conceptually similar, were established with different targets: separation of plume bending regimes in the case of Π and accuracy in plume height estimation in the case of τ^*. As such, Π can be expected to be associated with large uncertainty in H_P and small uncertainty in θ_P, while the opposite is true for τ^*. Results here partially agree with this categorization.

In the case of the plume height, median values per group show a nonlinear change depending on the logarithm of Π, with the IQR increasing with increasing log(Π) values (Figure 11a). On the other hand, H_P increases almost linearly with an decrease in the logarithm of τ^*, with the IQR remaining relatively small for

all groups (Figure 11b). Maximum plume height values are also better sorted when using τ^*, but the trend is not as clear as the median and average values.

Results for the plume angles are largely similar for both Π and τ^* (Figures 11c and 11d). An exception here is the lowermost group in the case of Π ($\log(\Pi) > 0.39$) which is associated with a small uncertainty of the plume angle. Overall, there is only a 1° difference in the average IQR between the calculations for the two parameters, revealing a very small decrease of uncertainty in the case of Π.

As far as the categorization between the three plume regimes, it can be seen that the threshold values based on Carazzo et al. (2014) seem to be appropriate for the set of the vulcanian eruptions studied here. For $\Pi < 0.06$ the median plume angle is $\leq$30° and the associated median plume heights are $\leq$1,800 m, while for $\Pi > 0.2$ median plume angles are over 60°, with heights 2,100 m. Similar results can be seen using τ^* values of 0.02 and 0.08, which separate the data between the same plume angles but with median plume heights less that 1,700 and over 2,200 m.

Despite some differences in the results, in the context of the study and lacking accurate direct measurements, the two parameters provide largely similar results. This could be explained due to the uncertainties of the data involved—predominately U, U_0, and the TGSD. The wind field is known to change due to the effect of topography (e.g., Poulidis et al., 2017) as well as due to the time difference between the eruption and the sounding. In the calculations here U_0 was based on FPLUME output but the exit velocity at the vent was arbitrarily set at 120 m/s. Finally, the TGSD is known to affect plume height (Michaud-Dubuy et al., 2018), but this effect was ignored due to the lack of data. For a more detailed approach on the subject, FPLUME would need to be coupled with a numerical weather prediction model to allow for high-resolution computational experiments to mirror the controlled nature of analog experiments (e.g., Carazzo et al., 2014).

5. Summary and Conclusions

The recent eruptive activity from Sakurajima volcano allows for the comprehensive study of small to moderate eruptions. Here, 1-D plume modeling using the FPLUME model was employed in order to compare MFR estimation methods and gain new insight on the effect of atmospheric stability parameters on the rise of volcanic plume from vulcanian eruptions.

Simulations using the FPLUME model were seen to be realistic and as expected for the given background conditions. However, results need to be scrutinized under unstable atmospheric conditions as the model either failed to provide a solution or was seen to overestimate the plume height; an issue that might persist for other similar 1-D models. In these cases, a simple estimate of the plume height using analytical solutions might be better at providing an accurate solution that can be used to run a TTDD model; however, this comes at the cost of resolving the plume shape, which in turn has an effect on the accuracy of the volcanic ash dispersal modeling (Poulidis et al., 2019).

The main conclusions of the study are as follows:

- Despite differences in the formulation, mass flow rate estimates provided by analytical expressions, modeling, and geophysical signal analysis carried out by the Sakurajima observatory were seen to provide complementing results, with the latter providing appropriate lower and upper first guess data.
- FPLUME was seen to provide realistic plume results for a number of different eruptive and atmospheric conditions, with the exception of some cases that featured pronounced convective instability in the atmosphere, when analytical expressions where seen to provide more consistent estimates.
- Although uncertainties and variations in the other source parameters are inevitable, the model sensitivity for the typical eruptions from Sakurajima was seen to be low, leading to a ~10% error in the associated output from the model.
- The plume scaling parameter Π (a relative measure of wind effects on the plume) was seen to be a robust metric in categorizing volcanic plumes from vulcanian eruptions from Sakurajima into three plume regimes (weak, transitional, strong), but the categorization is associated with relatively large uncertainty over the final plume height.
- Three commonly used atmospheric structure metrics, vertical wind speed shear, vertical wind direction shear, and the lifted index were seen to affect plume morphology by modifying plume height and plume angle, providing some disambiguation for cases with similar Π but different plume characteristics.

- Calculating the minimum Π for different layers along the plume height can be useful in assessing the importance of layers with significant shear.

The ESPs along with the associated atmospheric background characteristics has been compiled as a database and made available here (Data Sets S1 and S2) for further analysis and experiments.

Acknowledgments
This work was supported by the Integrated Program for the Next Generation Volcano Research and Human Resource Management project funded by the Japan Ministry of Education, Culture, Sports, Science and Technology (MEXT). Atmospheric sounding data were retrieved from the University of Wyoming archive. The database, full FPLUME results, and any other relevant data used in the study have been included as supporting information and can be freely accessed from the journal website. The authors declare that they have no conflict of interest. The authors would like to thank two anonymous reviewers for their helpful comments and suggestions.

References

Aramaki, S. (1984). Formation of the Aira Caldera, southern Kyushu, ~22,000 years ago. *Journal of Geophysical Research*, *89*, 8485–8501. https://doi.org/10.1029/JB089iB10p08485

Bagheri, G., Rossi, E., Biass, S., & Bonadonna, C. (2016). Timing and nature of volcanic particle clusters based on field and numerical investigations. *Journal of Volcanology and Geothermal Research*, *327*, 520–530. https://doi.org/10.1016/j.jvolgeores.2016.09.009

Biass, S., Todde, A., Cioni, R., Pistolesi, M., Geshi, N., & Bonadonna, C. (2017). Potential impacts of tephra fallout from a large-scale explosive eruption at Sakurajima volcano. *Japan Bulletin of Volcanology*, *79*, 73. https://doi.org/10.1007/s00445-017-1153-5

Blanchard, D. O. (1998). Assessing the vertical distribution of convective available potential energy. *Weather and Forecasting*, *13*, 870–877. https://doi.org/10.1175/1520-0434(1998)013<0870:atvdoc>2.0.co;2

Bonadonna, C., & Phillips, J. C. (2003). Sedimentation from strong volcanic plumes. *Journal of Geophysical Research*, *108*(B7), 2340. https://doi.org/10.1029/2002JB002034

Bonadonna, C., Pistolesi, M., Degruyter, W., Elissondo, M., & Baumann, V. (2015). Dynamics of wind-affected volcanic plumes: The example of the 2011 Cordón Caulle eruption, Chile. *Journal of Geophysical Research: Solid Earth*, *120*, 2242–2261. https://doi.org/10.1002/2014JB011478

Briggs, G. A. (1972). Chimney plumes in neutral and stable surroundings. *Atmospheric Environment*, *6*, 507–510. https://doi.org/10.1016/0004-6981(72)90120-5

Brown, R. J., Bonadonna, C., & Durant, A. J. (2012). A review of volcanic ash aggregation. *Physics and Chemistry of the Earth*, *45–46*, 65–78. https://doi.org/10.1016/j.pce.2011.11.001

Bursik, M. (2001). Effect of wind on the rise height of volcanic plumes. *Geophysical Research Letters*, *28*, 3621–3624. https://doi.org/10.1029/2001GL013393

Carazzo, G., Girault, F., Aubry, T., Bouquerel, H., & Kaminski, E. (2014). Laboratory experiments of forced plumes in a density-stratified crossflow and implications for volcanic plumes. *Geophysical Research Letters*, *41*, 8759–8766. https://doi.org/10.1002/2014GL061887

Clarke, A. B., Voight, B., Neri, A., & Macedonio, G. (2002). Transient dynamics of vulcanian explosions and column collapse. *Nature*, *415*, 897–901. https://doi.org/10.1038/415897a

Costa, A., Folch, A., & Macedonio, A. (2010). A model for wet aggregation of ash particles in volcanic plumes and clouds: 1. Theoretical formulation. *Journal of Geophysical Research*, *115*, B09201. https://doi.org/10.1029/2009JB007175

Costa, A., Macedonio, G., & Folch, A. (2006). A three-dimensional Eulerian model for transport and deposition of volcanic ashes. *Earth and Planetary Science Letters*, *241*, 634–647. https://doi.org/10.1016/j.epsl.2005.11.019

Costa, A., Suzuki, Y. J., Cerminara, M., Devenish, B. J., Esposti Ongaro, T., Herzog, M., et al. (2016). Results of the eruptive column model inter-comparison study. *Journal of Volcanology and Geothermal Research*, *326*, 2–25. https://doi.org/10.1016/j.jvolgeores.2016.01.017

de'Michieli Vitturi, M., Neri, A., & Barsotti, S. (2015). PLUME-MoM 1.0: A new integral model of volcanic plumes based on the method of moments. *Geoscientific Model Development*, *8*, 2447–2463. https://doi.org/10.5194/gmd-8-2447-2015

Degruyter, W., & Bonadonna, C. (2012). Improving on mass flow rate estimates of volcanic eruptions. *Geophysical Research Letters*, *39*, L16308. https://doi.org/10.1029/2012GL052566

Degruyter, W., & Bonadonna, C. (2013). Impact of wind on the condition for column collapse of volcanic plumes. *Earth and Planetary Science Letters*, *377*, 218–226. https://doi.org/10.1016/j.epsl.2013.06.041

Devenish, B. J. (2013). Using simple plume models to refine the source mass flux of volcanic eruptions according to atmospheric conditions. *Journal of Volcanology and Geothermal Research*, *256*, 118–127. https://doi.org/10.1016/j.jvolgeores.2013.02.015

Ernst, G. G. J., Sparks, R. S. J., Carey, S. N., & Bursik, M. I. (1996). Sedimentation from turbulent jets and plumes. *Journal of Geophysical Research*, *101*, 5575–5589. https://doi.org/10.1029/95JB01900

Esposti Ongaro, T, Cavazzoni, C., Erbacci, G., Neri, A., & Salvetti, M. (2007). A parallel multiphase flow code for the 3D simulation of explosive volcanic eruptions. *Parallel Computing*, *33*, 541–560. https://doi.org/10.1016/j.parco.2007.04.003

Folch, A. (2012). A review of tephra transport and dispersal models: Evolution, current status, and future perspectives. *Journal of Volcanology and Geothermal Research*, *235–236*, 96–115. https://doi.org/10.1016/j.jvolgeores.2012.05.020

Folch, A., Costa, A., & Macedonio, G. (2009). FALL3D: A computational model for transport and deposition of volcanic ash. *Computers & Geosciences*, *35*, 1334–1342. https://doi.org/10.1016/j.cageo.2008.08.008

Folch, A., Costa, A., & Macedonio, G. (2016). FPLUME-1.0: An integral volcanic plume model accounting for ash aggregation. *Geoscientific Model Development*, *9*, 431–450. https://doi.org/10.5194/gmd-9-431-2016

Ganser, G. H. (1993). A rational approach to drag prediction of spherical and nonspherical particles. *Powder Technology*, *77*, 143–152. https://doi.org/10.1016/0032-5910(93)80051-B

Gilbert, J. S., & Lane, S. J. (1994). The origin of accretionary lapilli. *Bulletin of Volcanology*, *56*, 398–411. https://doi.org/10.1007/BF00326465

Girault, F., Carazzo, G., Tait, S., Ferrucci, F., & Kaminski, E. (2014). The effect of total grain-size distribution on the dynamics of turbulent volcanic plumes. *Earth and Planetary Science Letters*, *394*, 124–134. https://doi.org/10.1016/j.epsl.2014.03.021

Girault, F., Carazzo, G., Tait, S., & Kaminski, E. (2016). Combined effects of total grain-size distribution and crosswind on the rise of eruptive volcanic columns. *Journal of Volcanology and Geothermal Research*, *326*, 103–113. https://doi.org/10.1016/j.jvolgeores.2015.11.007

Hansell, A., & Oppenheimer, C. (2004). Health hazards from volcanic gases: A systematic literature review. *Archives of Environmental Health: An International Journal*, *59*, 628–639. https://doi.org/10.1080/00039890409602947

Hasegawa, Y., Sugai, A., Hayashi, Y., Hayashi, S., Saito, S., & Shimbori, T. (2015). Improvements of volcanic ash fall forecasts issued by the Japan Meteorological Agency. *Journal of Applied Volcanology*, *4*, 1–12. https://doi.org/10.1186/s13617-014-0018-2

Herzog, M., & Graf, H.-F. (2010). Applying the three-dimensional model ATHAM to volcanic plumes: Dynamic of large co-ingibrite eruptions and associated injection heights for volcanic gases. *Geophysical Research Letters*, *37*, L19807. https://doi.org/10.1029/2010GL044986

Hillman, S. E., Horwell, C. J., Densmore, A. L., Damby, D. E., Fubini, B., Ishimine, Y., & Tomatis, M. (2012). Sakurajima volcano: A physico-chemical study of the health consequences of long-term exposure to volcanic ash. *Bulletin of Volcanology*, *74*, 913–930. https://doi.org/10.1007/s00445-012-0575-3

Horwell, C., & Baxter, P. (2006). The respiratory health hazards of volcanic ash: A review for volcanic risk mitigation. *Bulletin of Volcanology*, *69*, 1–24. https://doi.org/10.1007/s00445-006-0052-y

Iguchi, M. (2016). Method for real-time evaluation of discharge rate of volcanic ash—Case study on intermittent eruptions at the Sakurajima volcano, Japan. *Journal of Disaster Research*, *11*, 4–13. https://doi.org/10.20965/jdr.2016.p0004

Iguchi, M., Tameguri, T., Ohta, Y., Ueki, S., & Nakao, S. (2013). Characteristics of volcanic activity at Sakurajima volcano's Showa Crater during the period 2006 to 2011. *Bulletin of the Volcanological Society of Japan*, *58*, 115–135. https://doi.org/10.18940/kazan.58.1_115

Iguchi, M., Yakiwara, H., Tameguri, T., Hendrasto, M., & Hirabayashi, J. (2008). Mechanism of explosive eruption revealed by geophysical observations at the Sakurajima, Suwanosejima and Semeru volcanoes. *Journal of Volcanology and Geothermal Research*, *178*, 1–9. https://doi.org/10.1016/j.jvolgeores.2007.10.010

Ishihara, K. (1985). Dynamical analysis of volcanic explosion. *Journal of Geodynamics*, *3*, 327–349. https://doi.org/10.1016/0264-3707(85)90041-9

Jenkins, S. F., Wilson, T. M., Magill, C. R., Miller, V., Stewart, C., Blong, R., et al. (2015). Volcanic ash fall hazard and risk. In S. C. Loughlin, R. S. J. Sparks, S. K. Brown, S. F. Jenkins, & C. Vye-Brown (Eds.), *Global Volcanic Hazards and Risk* (pp. 173–222). Cambridge: Cambridge Academic Press. https://doi.org/10.1017/CBO9781316276273

Kaminski, E., Tait, S., & Carazzo, G. (2005). Turbulent entrainment in jets with arbitrary buoyancy. *Journal of Fluid Mechanics*, *526*, 361–376. https://doi.org/10.1017/S0022112004003209

Kinoshita, K. (1996). Observation of flow and dispersion of volcanic clouds from Mt. Sakurajima. *Atmospheric Environment*, *30*, 2831–2837. https://doi.org/10.1016/1352-2310(95)00401-7

Lähde, A., Gudmundsdottir, S. S., Joutsensaari, J., Tapper, U., Ruusunen, J., Ihalainen, M., et al. (2013). In vitro evaluation of pulmonary deposition of airborne volcanic ash. *Atmospheric Environment*, *70*, 18–27. https://doi.org/10.1016/j.atmosenv.2012.12.048

Macedonio, G., Costa, A., & Folch, A. (2016). Uncertainties in volcanic plume modeling: A parametric study using FPLUME. *Journal of Volcanology and Geothermal Research*, *326*, 92–102. https://doi.org/10.1016/j.jvolgeores.2016.03.016

Mastin, L. G. (2007). A user-friendly one-dimensional model for wet volcanic plumes. *Geochemistry, Geophysics,Geosystems*, *8*, Q03014. https://doi.org/10.1029/2006GC001455

Mastin, L. G., Guffanti, M., Servranckx, R., Webley, P., Barsotti, S., Dean, K., et al. (2009). A multidisciplinary effort to assign realistic source parameters to models of volcanic ash-cloud transport and dispersion during eruptions. *Journal of Volcanology and Geothermal Research*, *186*, 10–21. https://doi.org/10.1016/j.jvolgeores.2009.01.008

Michaud-Dubuy, A., Carazzo, G., Kaminski, E., & Girault, F. (2018). A revisit of the role of gas entrapment on the stability conditions of explosive volcanic columns. *Journal of Volcanology and Geothermal Research*, *357*, 349–361. https://doi.org/10.1016/j.jvolgeores.2018.05.005

Michaud-Dubuy, A., Carazzo, G., Tait, S., Le Hir, G., Fluteau, F., & Kaminski, E. (2019). Impact of wind direction variability on hazard assessment in Martinique (Lesser Antilles): The example of the 13.5 ka cal BP Bellefontaine Plinian eruption of Mount Pelée volcano. *Journal of Volcanology and Geothermal Research*, *381*, 193–208. https://doi.org/10.1016/j.jvolgeores.2019.06.004

Morrissey, M. M., & Mastin, L. G. (2000). Vulcanian eruptions. In H. Sigurdsson (Ed.), *Encyclopedia of Volcanoes* (pp. 463–476). San Diego, California: Academic. https://doi.org/10.1016/B978-0-12-385938-9.00028-6

Morton, B. R., Taylor, G. I., & Turner, J. S (1956). Turbulent gravitational convection from maintained and instantaneous source. *Proceedings of the Royal Society of London A*, *234*, 1–23. https://doi.org/10.1098/rspa.1956.0011

Newhall, C. G., & Self, S. (1982). The volcanic explosivity index (VEI) an estimate of explosive magnitude for historical volcanism. *Journal of Geophysical Research*, *87*, 1231–1238. https://doi.org/10.1029/JC087iC02p01231

Poulidis, A. P., Phillips, J. C., Renfrew, I. A., Barclay, J., Hogg, A., Jenkins, S. F., et al. (2018). Meteorological controls on local and regional volcanic ash dispersal. *Scientific Reports*, *8*, 6873. https://doi.org/10.1038/s41598-018-24651-1

Poulidis, A. P., & Takemi, T. (2017). A 1998–2013 climatology of Kyushu, Japan: Seasonal variations of stability and rainfall. *International Journal of Climatology*, *37*, 1843–1858. https://doi.org/10.1002/joc.4817

Poulidis, A. P., Takemi, T., & Iguchi, M. (2019). Experimental high-resolution forecasting of volcanic ash hazard at Sakurajima, Japan. *Journal of Disaster Research*, *14*, 786–797. https://doi.org/10.20965/jdr.2019.p0786

Poulidis, A. P., Takemi, T., Iguchi, M., & Renfrew, I. A (2017). Orographic effects on the transport and deposition of volcanic ash: A case study of Mount Sakurajima Japan. *Journal of Geophysical Research: Atmospheres*, *122*, 9332–9350. https://doi.org/10.1002/2017JD026595

Poulidis, A. P., Takemi, T., Shimizu, A., Iguchi, M., & Jenkins, S. F. (2018). Statistical analysis of dispersal and deposition patterns of volcanic emissions from Mt. Sakurajima, Japan. *Atmospheric Environment*, *179*, 305–320. https://doi.org/10.1016/j.atmosenv.2018.02.021

Shimbori, T., Sakurai, T., Tahara, M., & Fukui, K. (2013). Observation of eruption clouds with weather radars and meteorological satellites: A case study of the eruptions at Shinmoedake volcano in 2011. *Quarterly Journal of Seismology*, *77*, 139–214.

Sparks, R. S. J. (1986). The dimensions and dynamics of volcanic eruption columns. *Bulletin of Volcanology*, *114*, B03209. https://doi.org/10.1007/BF01073509

Sparks, R. S. J., Bursik, M. I., Carey, S. N., Gilbert, J. S., Glaze, L. S., Sigurdsson, H., & Woods, A. W. (1997). *Volcanic plumes* (pp. 574). Chichester: John Wiley.

Suwa, H., Suzuki, Y. J., & Yooko, A. (2014). Estimation of exit velocity plume from analysis of vortex structures. *Earth and Planetary Science Letters*, *385*, 154–161. https://doi.org/10.1016/j.epsl.2013.10.032

Suzuki, Y. J., & Koyaguchi, T. (2009). A three-dimensional numerical simulation of spreading umbrella clouds. *Journal of Geophysical Research*, *114*, B03209. https://doi.org/10.1029/2007JB005369

Suzuki, Y. J., & Koyaguchi, T. (2013). 3D numerical simulation of volcanic eruption clouds during the 2011 Shinmoe-dake eruptions. *Earth, Planets and Space*, *65*, 581–589. https://doi.org/10.5047/eps.2013.03.009

Suzuki, Y. J., & Koyaguchi, T. (2015). Effects of wind on entrainment efficiency in volcanic plumes. *Journal of Geophysical Research: Solid Earth*, *120*, 6122–6140. https://doi.org/10.1002/2015JB012208

Suzuki, Y. J., Koyaguchi, T., Ogawa, M., & Hachisu, I. (2005). A numerical study of turbulent behaviour in eruption clouds using a three-dimensional fluid dynamics model. *Journal of Geophysical Research*, *110*, B08201. https://doi.org/10.1029/2004JB003460

Tate, P. M. (2002). The rise and dilution of buoyant jets and their behaviour in an internal wave field (PhD Thesis), University of New South Wales.

Tate, P. M., & Middleton, J. H. (2000). Unification of non-dimensional solutions to asymptotic equations for plumes of different shape. *Boundary-Layer Meteorology*, *94*, 225–251. https://doi.org/10.1023/A:1002431928523

Todde, A., Cioni, R., Pistolesi, M., Geshi, N., & Bonadonna, C. (2017). The 1914 Taisho eruption of Sakurajima volcano: Stratigraphy and dynamics of the largest explosive event in Japan during the twentieth century. *Bulletin of Volcanology*, *79*, 72. https://doi.org/10.1007/s00445-017-1154-4

Tournigand, P.-Y., Taddeucci, J., Gaudin, D., Peña Fernández, J. P., Bello, D. E., Scarlato, P., et al. (2017). The initial development of transient volcanic plumes as a function of source conditions. *Journal of Geophysical Research: Solid Earth*, *122*, 9784–9803. https://doi.org/10.1002/2017JB014907

Turner, J. S. (1969). Buoyant plumes and thermals. *Annual Review in Fluid Mechanics*, *1*, 29–44. https://doi.org/10.1146/annurev.fl.01.010169.000333

Vergniolle, S., & Mangan M. (2000). Hawaiian and Strombolian eruptions. In H. Sigurdsson (Ed.), *Encyclopedia of volcanoes* (pp. 447–461). San Diego, California: Academic. https://doi.org/10.1016/B978-0-12-385938-9.00027-4

Wilson, L., Sparks, R. S. J., Huang, T. C., & Watkins, N. D. (1978). The control of volcanic column heights by eruption energetics and dynamics. *Journal of Geophysical Research*, *83*, 1829–1836. https://doi.org/10.1029/JB083iB04p01829

Wilson, T. M., Stewart, C., Sword-Daniels, V., Leonard, G. S., Johnston, D. M., Cole, J. W., et al. (2012). Volcanic ash impacts on critical infrastructure. *Physics and Chemistry of the Earth, Parts A/B/C*, *45–46*, 5–23. https://doi.org/10.1016/j.pce.2011.06.006

Woodhouse, M. J., Hogg, A. J., & Phillips, J. C. (2016). A global sensitivity analysis of the PlumeRise model of volcanic plumes. *Journal of Volcanology and Geothermal Research*, *326*, 54–76. https://doi.org/10.1016/j.jvolgeores.2016.02.0192

Woodhouse, M. J., Hogg, A. J., Phillips, J. C., & Sparks, R. S. J. (2013). Interaction between volcanic plumes and wind during the 2010 Eyjafjallajökull eruption, Iceland. *Journal of Geophysical Research: Solid Earth*, *118*, 92–109. https://doi.org/10.1029/2012JB009592

Woods, A. W. (1988). The fluid dynamics and thermodynamics of eruption plumes. *Bulletin of Volcanology*, *50*, 169–193. https://doi.org/10.1007/BF01079681

Woods, A. W. (1993). Moist convection and the injection of volcanic ash into the atmosphere. *Journal of Geophysical Research*, *98*, 17627. https://doi.org/10.1029/93JB00718